

## NUMERICAL SIMULATION OF DENSITY EVOLUTION OF DUST AGGREGATES IN PROTOPLANETARY DISKS. I. HEAD-ON COLLISIONS

TORU SUYAMA, KOJI WADA, AND HIDEKAZU TANAKA

Institute of Low Temperature Science, Hokkaido University, N19-W8, Sapporo 060-0819, Japan; storu@neko.lowtem.hokudai.ac.jp

Received 2008 March 2; accepted 2008 May 15

### ABSTRACT

The bulk density of dust aggregates is an important factor in collisional growth of dust in protoplanetary disks. The density of aggregates changes the coupling with the disk gas, which governs the motion of aggregates in disks. Collisional outcomes also depend on the aggregate density. We perform three-dimensional  $N$ -body simulations of sequential collisions of aggregates composed of a number of submicron-sized icy particles in order to investigate the density evolution of dust aggregates growing in protoplanetary disks. In the present simulation of sequential collisions, as the initial aggregates at each collision, we use the resultant aggregate obtained at the previous collision. By repeating  $N$ -body calculations of aggregate collisions, we examined the density evolution of aggregate collisions. At an early stage of dust growth, aggregates stick to each other without restructuring, and the density of these aggregates decreases. At a later stage, in which the impact energy exceeds a critical energy, aggregates are gradually compressed. The compressed aggregates have a fractal dimension of 2.5. Because of this small fractal dimension, their density remains very low even at this compression stage. We also derive an equation describing the density evolution of growing aggregates. Applying this equation to dust growth in protoplanetary disks, we find that dust aggregates have an extremely low density ( $< 0.1 \text{ kg m}^{-3}$ ). In the simulation of the present study, we consider only head-on collisions. The effect of oblique collisions would further reduce the aggregate density.

*Subject headings:* circumstellar matter — dust, extinction — methods:  $n$ -body simulations —  
 planetary systems: formation — planetary systems: protoplanetary disks

### 1. INTRODUCTION

Planetary systems are believed to have formed in protoplanetary disks through mutual collisions and coalescence of planetesimals. Planetesimals are made from dust aggregates in protoplanetary disks. Dust aggregates grow through mutual collisions and gradually settle to the midplane of a disk, which forms a dense dust layer at the midplane (e.g., Safronov 1969; Nakagawa et al. 1981). Planetesimals would be formed in the dense dust layer through gravitational instability (e.g., Goldreich & Ward 1973) or simple coalescence (e.g., Weidenschilling & Cuzzi 1993). It has been suggested that the dust layer cannot be dense enough for the gravitational instability because of turbulent gaseous motion caused by shear instability (e.g., Weidenschilling & Cuzzi 1993). Thus, coupling between dust aggregates and disk gas is an important factor in the planetesimal formation processes. This coupling is governed by the internal structure of dust aggregates. The sticking probability and the disruption at aggregate collisions are also important in dust growth. The collisional outcomes would also be closely related to the aggregate structure.

Most previous studies on dust growth in protoplanetary disks neglected the internal structure of aggregates and assumed compact aggregates with a constant density (e.g., Safronov 1969; Weidenschilling 1980; Nakagawa et al. 1981). Some studies took into account the internal structure of dust aggregates (e.g., Ossenkopf 1993; Kempf et al. 1999; Blum 2004; Ormel et al. 2007). As reviewed by Blum (2004) the structural evolution of dust aggregates is described as follows. At the early stage of dust growth in protoplanetary disks, dust aggregates of micron size are strongly coupled with disk gas (e.g., Adachi et al. 1976), which leads to a significantly low impact velocity between aggregates ( $< 1 \text{ mm s}^{-1}$ ). In such a low-velocity collision, aggregates would simply stick without any restructuring, resulting in clusters of ballistic cluster-cluster aggregation (BCCA; e.g., Meakin 1991). The BCCA

clusters have a very fluffy structure with a fractal dimension of 1.5–2 (Mukai et al. 1992; Krause & Blum 2004; Paszun & Dominik 2006). As dust aggregates grow, the impact energy increases. When the impact energy becomes large enough, aggregates are expected to be compressed and become relatively compact. Ormel et al. (2007) examined the density evolution of dust aggregates more quantitatively with their simple model of aggregate compression. However, the aggregate compression should be further investigated by both theoretical and experimental studies.

Many authors performed various experiments of aggregate collisions (e.g., Poppe et al. 2000; Blum & Wurm 2000; Wurm et al. 2005; Paraskov et al. 2007). Such experimental studies help to clarify the aggregate structure. Theoretical study is also a powerful tool for modeling the structure evolution. Dominik & Tielens (1997) performed two-dimensional numerical simulations of aggregate collisions, using a particle interaction model developed by their group (Chokshi et al. 1993; Dominik & Tielens 1995, 1996). They derived a simple recipe for the outcomes of aggregate collisions, i.e., compression and disruption. Recently, Wada et al. (2007, 2008, hereafter W07, W08) performed two-dimensional (2D) and three-dimensional (3D) simulations of head-on collisions of BCCA clusters composed of up to thousands of particles. Their results confirmed Dominik & Tielens' recipe. In both 2D and 3D cases, they obtained empirical scaling laws for the size of compressed aggregates as functions of the impact energy. In the 3D case, W08 found that the fractal dimension of compressed aggregates is  $\simeq 2.5$  although Ormel et al. (2007) assumed the fractal dimension to be 3 in their simple model. W08 also introduced the effective pressure of aggregates as a function of the density and the number of particles in aggregates and succeeded in reproducing the scaling for the compression of 3D aggregates with the use of the effective pressure. Using the effective pressure, we would be able to examine the density evolution of dust growing in protoplanetary disks. However, W08 considered aggregate

compression at only single collision although aggregates grow through successive collisions in protoplanetary disks. Because of successive collisions, the properties of compressed aggregates, such as the fractal dimension and the effective pressure, can deviate from those obtained by W08.

In the present paper, we perform 3D simulations of sequential aggregate collisions and examine the density evolution of aggregates growing through collisions. The simulation starts from a collision of aggregates composed of two particles (i.e., dimers). As the initial aggregates at each collision, we use the resultant aggregate obtained in the previous collision. By repeating such calculations of aggregate collisions, we will investigate a more realistic compression process during aggregate growth. Comparing our results with those of W08, we examine the validity of their compression model.

In § 2, we describe the numerical procedure of our simulation of sequential aggregate collisions. In § 3, we present our numerical results on the density evolution of growing aggregates. In § 4, we compare our results with those of W08. We also derive an equation describing the density evolution of growing aggregates. Although we consider only icy aggregates in our simulation, the derived equation would be applicable to silicate aggregates. In § 5, we apply our results to dust growth in protoplanetary disks. We find that dust aggregates have an extremely low density in protoplanetary disks because of the ineffectiveness of collisional compression. A summary is given in § 6.

## 2. NUMERICAL PROCEDURE

### 2.1. *N*-Body Calculation of Aggregate Collisions

By repeating the calculation of an aggregate collision, we describe the growth of aggregates. We perform 3D *N*-body calculations of aggregate collisions in the same way as W08. Here, we briefly summarize the numerical procedure of the *N*-body calculation. We consider aggregates consisting of a number of spherical icy particles with a radius of  $0.1 \mu\text{m}$ . We calculate the motion of individual particles, by integrating the equations of motion for each particle. The equations of motion for the translational and rotational motions of the *i*th particle are given by

$$m_i \frac{d\mathbf{v}_i}{dt} = \sum_j \mathbf{F}_{ij}, \quad (1)$$

$$I_i \frac{d\boldsymbol{\omega}_i}{dt} = \sum_j \mathbf{M}_{ij}, \quad (2)$$

where  $m_i$ ,  $I_i$ ,  $\mathbf{v}_i$ , and  $\boldsymbol{\omega}_i$  are the mass, the moment of inertia, the velocity, and the angular velocity of the particle *i*, respectively, and  $\mathbf{F}_{ij}$  and  $\mathbf{M}_{ij}$  are the force and the torque exerted on the particle *i* by the particle *j*, respectively. The summations in the right-hand sides are taken over all particles in contact with particle *i*. The position  $\mathbf{x}_i$  of the particle *i* is calculated, by integrating the velocity  $\mathbf{v}_i$ . To describe the rotation of the particle *i*, we use the Eulerian parameters  $e_{0,i}$  and  $\mathbf{e}_i = (e_{1,i}, e_{2,i}, e_{3,i})$  as well as W07 and W08. The Eulerian parameters are integrated with the equations<sup>1</sup> (e.g., Goldstein 1950)

$$\frac{de_{0,i}}{dt} = -\frac{1}{2} \mathbf{e}_i \cdot \boldsymbol{\omega}_i, \quad (3)$$

$$\frac{d\mathbf{e}_i}{dt} = \frac{1}{2} (e_{0,i} \boldsymbol{\omega}_i - \mathbf{e}_i \times \boldsymbol{\omega}_i). \quad (4)$$

Each particle is considered as an elastic sphere having the surface energy. For icy particles, the surface energy  $\gamma$  is set to be  $0.1 \text{ J m}^{-2}$ . Young's modulus  $E$  is 7 GPa and Poisson's ratio  $\nu$  is 0.25. The material density  $\rho_m$  is  $1000 \text{ kg m}^{-3}$ . These values are the same as in W07 and W08. When two particles are in contact, their elasticity produces a repulsive force between them, and the surface energy causes an attractive force. The repulsive and the attractive forces in the normal direction are formulated by Johnson et al. (1971). Furthermore, when two particles in contact slide, roll, or twist in relation to one another, tangential forces and torques arise that resist the motions. These forces and torques are formulated by Dominik & Tielens (1995, 1996). W07 introduced the potential energies that give these forces and torques to ensure conservation of total energy in the case of no energy dissipation. In our simulation, we use their model. The force  $\mathbf{F}_{ij}$  and the torque  $\mathbf{M}_{ij}$  exerted on the particle *i* by the particle *j* are expressed as

$$\mathbf{F}_{ij} = \mathbf{F}_{n,ij} + \mathbf{F}_{s,ij}, \quad (5)$$

$$\mathbf{M}_{ij} = \mathbf{M}_{s,ij} + \mathbf{M}_{r,ij} + \mathbf{M}_{t,ij}, \quad (6)$$

where  $\mathbf{F}_{n,ij}$  is the force due to normal motion,  $\mathbf{F}_{s,ij}$  and  $\mathbf{M}_{s,ij}$  are the force and the torque, respectively, due to sliding motion, and  $\mathbf{M}_{r,ij}$  and  $\mathbf{M}_{t,ij}$  are the torques due to rolling and twisting motions, respectively. The normal force  $\mathbf{F}_{n,ij}$  depends on the compressive length  $\delta$ , which is defined by  $2r_1 - |\mathbf{x}_i - \mathbf{x}_j|$ . Note that all monomer particles are assumed to have the same radius  $r_1$  ( $=0.1 \mu\text{m}$ ) and the same mass  $m_1$  ( $=4.2 \times 10^{-18} \text{ kg}$ ). At the moment of separation,  $\delta$  is equal to a critical value,  $-\delta_{\text{crit}}$ , given by  $-(1/6)^{1/3} a_0^2 / r_1$ , where  $a_0$  is the radius of the contact surface area at the equilibrium state given by  $[9\pi\gamma r_1^2 (1 - \nu^2) / (2E)]^{1/3}$ . For icy particles,  $\delta_{\text{crit}}$  is  $8.4 \text{ \AA}$ .

When the displacements due to sliding, rolling, or twisting motions exceed critical values, the interaction between the two contact particles enters the inelastic regime, which is accompanied by energy dissipation. We consider the inelastic regime as described in W07. Aggregates are compressed through mainly inelastic rolling motion (Dominik & Tielens 1997; W07, W08). The (inelastic) rolling energy  $E_{\text{roll}}$  is that required for rolling with a distance  $(\pi/2)r_1$ . In W07, the rolling energy is given by

$$E_{\text{roll}} = 6\pi^2 \gamma r_1 \xi_{\text{crit}}, \quad (7)$$

where  $\xi_{\text{crit}}$  is the critical displacement for rolling. We need at least the energy  $E_{\text{roll}}$  to visibly restructure an aggregate. Dominik & Tielens (1995) set  $\xi_{\text{crit}}$  to be  $2 \text{ \AA}$ , whereas the experiments by Heim et al. (1999) suggested  $\xi_{\text{crit}} = 32 \text{ \AA}$  for  $1.8 \mu\text{m}$  sized  $\text{SiO}_2$  monomer particles. Because of this uncertainty, we deal with  $\xi_{\text{crit}}$  as a parameter.

In order to integrate the equations of motion, we use the leapfrog integrator as well as W07 and W08. This is a second-order symplectic integrator. The time step  $\Delta t$  is set to be  $0.058 \text{ ns}$  in all of our calculations. In our calculations, we consider  $\delta_{\text{crit}}$  to be the characteristic length. Since the fastest impact velocity  $v_{\text{imp,max}}$  is  $4.4 \text{ m s}^{-1}$  in our calculations, the characteristic time of our calculations,  $\delta_{\text{crit}} / v_{\text{imp,max}}$ , is  $0.19 \text{ ns}$ . Although  $\Delta t$  is not much smaller than this characteristic time, the energy error is less than  $0.01\%$  of the total energy because of the leapfrog integration scheme.

### 2.2. Simulation of Sequential Collisions

To examine the structure evolution of growing aggregates, we perform simulations of sequential collisions. The simulation

<sup>1</sup> Note that while eq. (32) in W07 does not have the minus sign, there should be the minus sign in the right-hand side of eq. (3). The equation in W07 is erroneous.

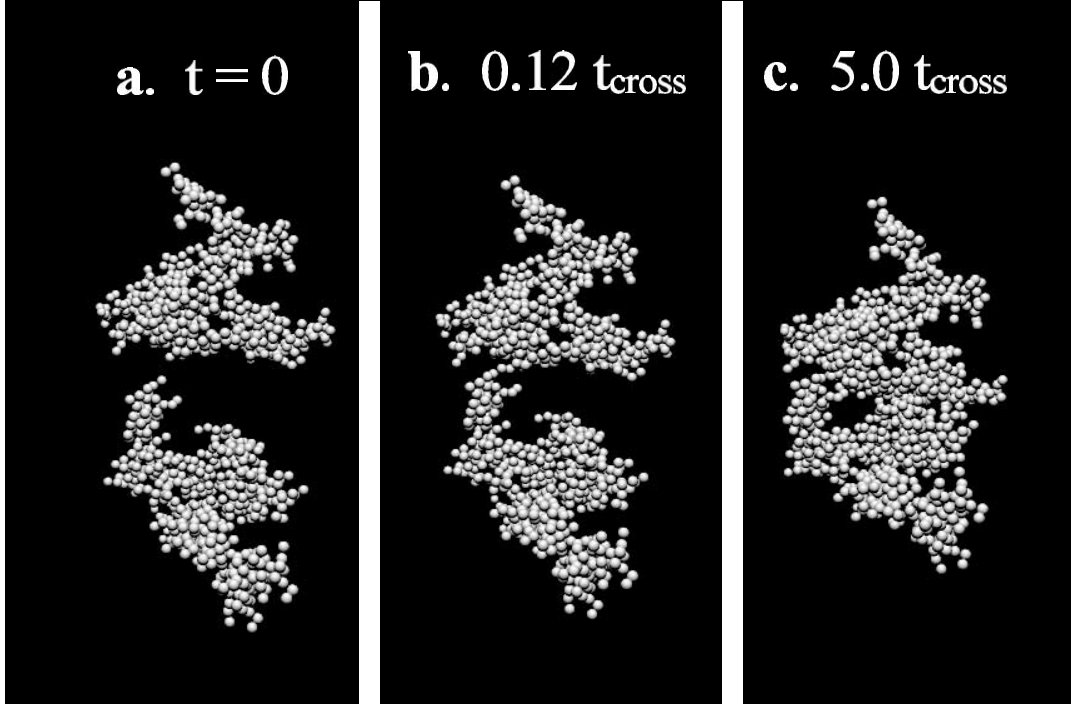


FIG. 1.— Snapshots of aggregates during a collision with  $v_{\text{imp}} = 0.54 \text{ m s}^{-1}$  and  $\xi_{\text{crit}} = 2 \text{ \AA}$  (a) before the collision, (b) at the moment of sticking, (c) and at the end of calculation. Initial aggregates are composed of 512 particles.

starts from a collision of aggregates composed of two particles (i.e., dimers) and ends with a collision of aggregates composed of 16,384 particles. As the initial aggregates at each collision, we prepare the resultant aggregate obtained in the previous collision and its copy rotated in a random direction. We consider only head-on collisions, as was the case in W07 and W08. Oblique collisions would create less compressed aggregates compared to head-on collisions. Thus, the bulk density of aggregates obtained in the present study is considered to be an upper limit. Since we are interested in the compression process, the impact velocity is set to be so low ( $< 5 \text{ m s}^{-1}$ ) that fragmentation should not occur in all collisional calculations. Thus, the aggregate mass is doubled at each collision.

The initial orientations of the aggregates are chosen randomly at each collision. Since the structure of a resultant aggregate at the collisional simulation depends on the initial orientation, we perform 30 runs for different sets of the initial orientations and take the average of each run. The  $N$ -body calculation of a collision starts just before the contact of the two aggregates at  $t = 0$  and lasts until  $t = 3t_{\text{cross}}$ . The crossing time  $t_{\text{cross}}$  is given by  $\Delta \mathbf{x}_{\text{crit}}/v_{\text{imp}}$ , where  $v_{\text{imp}}$  is the impact velocity and  $\Delta \mathbf{x}_{\text{crit}}$  is the initial separation between the centers of mass of the two aggregates. At the end of the calculation ( $t = 3t_{\text{cross}}$ ), inelastic dissipation almost terminates and the structure of the merged aggregate is almost fixed, but the aggregate still oscillates elastically. In protoplanetary disks, such a oscillation would be damped due to the gas drag force before the next collision. To damp this elastic oscillation in the  $N$ -body calculation, we carry out an additional integration after the above time range, by introducing artificial damping forces and torques to each particle. The damping force  $\mathbf{F}_{\text{damp},i}$  and the torque  $\mathbf{M}_{\text{damp},i}$  on the particle  $i$  are given by

$$\mathbf{F}_{\text{damp},i} = -C_{\text{damp}} m_1 \mathbf{v}_i, \quad (8)$$

$$\mathbf{M}_{\text{damp},i} = -C_{\text{damp}} I_1 \boldsymbol{\omega}_i, \quad (9)$$

where the coefficient  $C_{\text{damp}}$  is set to be  $8/t_{\text{cross}}$ . This additional calculation with damping is done from  $t = 3t_{\text{cross}}$  to  $5t_{\text{cross}}$ . As a result of this damping, the kinetic energy in the elastic oscillation is reduced to less than  $10^{-3}$  of that before the damping.

In the simulation of sequential collisions, for simplicity, the impact velocity  $v_{\text{imp}}$  is set to be constant at each collision. We perform the simulations for various values of  $v_{\text{imp}}$ , i.e., for 0.27, 0.54, 1.1, 2.2, and  $4.4 \text{ m s}^{-1}$ . The critical rolling displacement is another parameter, and we set  $\xi_{\text{crit}} = 2, 8, \text{ and } 16 \text{ \AA}$ .

### 3. RESULTS

Based on the procedure described in § 2.2, we perform simulations of sequential collisions. First, we show the outcomes of a collision with  $\xi_{\text{crit}} = 2 \text{ \AA}$  and  $v_{\text{imp}} = 0.54 \text{ m s}^{-1}$ . In this collision, the initial aggregates are composed of 512 particles. Figure 1 shows the collision. Figure 1a shows the initial condition. Figures 1b and 1c show the sticking and the end of the calculation, respectively. The total calculation time,  $5t_{\text{cross}}$ , corresponds to  $5.5 \text{ \mu s}$ . The resultant aggregate is compressed compared with that at the moment of sticking. In this calculation, the number of contact points in the aggregate increases by 8% from the initial value.

Figure 2 shows the time evolution of the kinetic energy and the dissipated energy in the above calculation. The kinetic energy decreases primarily due to the energy dissipation in the inelastic rolling motion. Because of the increase in the number of contact points, the binding energy of the merged aggregate also increases. As a result of this increase in the binding energy, the dissipated energy may exceed the impact energy. The energy dissipation almost terminates at  $t = t_{\text{cross}}$ , after which the kinetic energy is almost constant, except for its fluctuation. After  $t = 3t_{\text{cross}}$ , the artificial damping forces and torques are exerted, leading to a quick decrease in the kinetic energy.

In a series of sequential collisions, we repeat collisions of aggregates, using the resultant aggregate in the previous collision

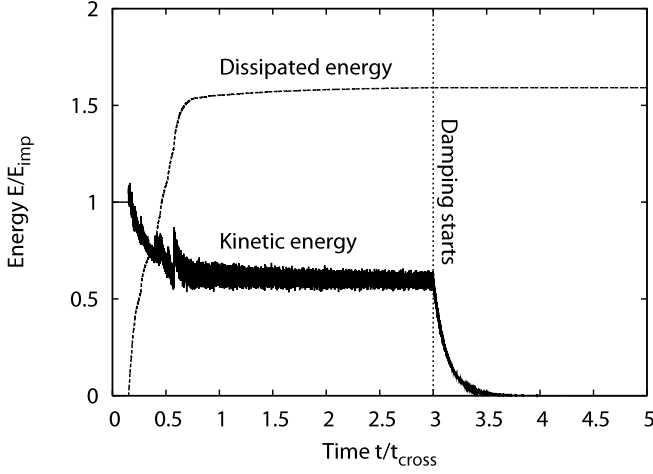


FIG. 2.—Time evolution of the kinetic energy (*solid line*) and the dissipated energy (*dashed line*) with  $v_{\text{imp}} = 0.54 \text{ m s}^{-1}$  and  $\xi_{\text{crit}} = 2 \text{ \AA}$ . At  $t = 3t_{\text{cross}}$ , the artificial damping forces and torques begin to be exerted.

as the initial condition. Figure 3 shows the resultant aggregates obtained from two series of sequential collisions. In the low-velocity case with  $v_{\text{imp}} = 0.54 \text{ m s}^{-1}$  (Fig. 3a), the resultant aggregates are fluffier than those in the high-velocity case with  $v_{\text{imp}} = 4.4 \text{ m s}^{-1}$  (Fig. 3b).

To examine the compression process quantitatively, we evaluate the radius or the volume of the resultant aggregates. We define the characteristic radius of an aggregate,  $r_{\text{crit}}$ , by (Mukai et al. 1992; W08)

$$r_{\text{crit}} \equiv \sqrt{\frac{5}{3}} r_g, \quad (10)$$

with the radius of gyration,  $r_g$ , given by

$$r_g \equiv \sqrt{\frac{\sum_{i=1}^N |\mathbf{x}_i - \mathbf{x}_M|^2}{N}}, \quad (11)$$

where  $\mathbf{x}_i$  is the position of particle  $i$ ,  $\mathbf{x}_M$  is the position of the center of mass of the aggregate, and  $N$  is the number of particles composing the aggregate. The volume  $V$  and the density  $\rho$  of the aggregate are evaluated with equations

$$V = \frac{4\pi}{3} r_{\text{crit}}^3, \quad (12)$$

$$\rho = \frac{m_1 N}{V}, \quad (13)$$

respectively.

Figure 4 shows the evolution of the radius and the density of the growing aggregates in the sequential collisions. The evolution curves of the radius and the density are not smooth in one run (see Figs. 4a and 4b), because aggregates collide with each other in random orientations. We perform 30 sequential collisions to obtain the averaged value. Figures 4c and 4d show the averaged radius and the averaged density, respectively, which give smooth evolution curves. The density of aggregates decreases on average as they grow.

Since aggregates are compressed through the inelastic rolling motion, the density evolution depends on the critical rolling

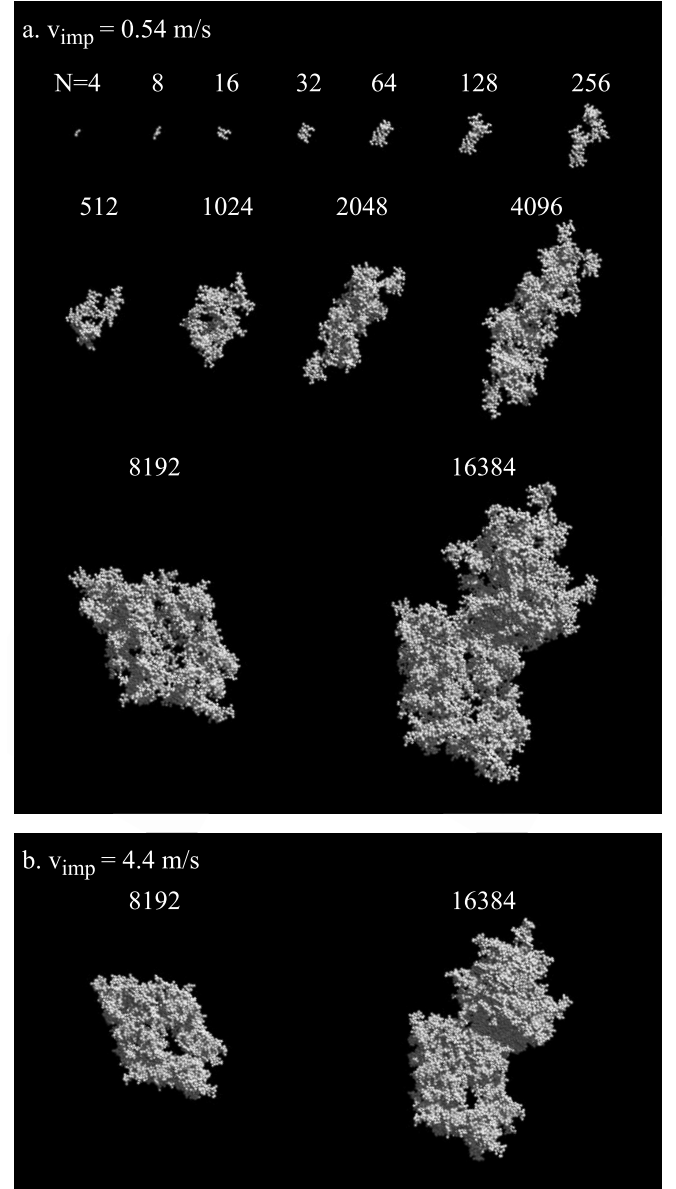


FIG. 3.—Resultant aggregates obtained from the simulations of sequential collisions with (a)  $v_{\text{imp}} = 0.54 \text{ m s}^{-1}$  and (b)  $v_{\text{imp}} = 4.4 \text{ m s}^{-1}$ . Aggregates obtained from the high-velocity case are more compact than those obtained from the low-velocity case.

energy  $E_{\text{roll}}$  (or  $\xi_{\text{crit}}$ , see eq. [7]) and the impact velocity  $v_{\text{imp}}$ . We performed similar simulations of sequential collisions for various values of parameters,  $\xi_{\text{crit}}$  and  $v_{\text{imp}}$ . Figure 5 shows the density evolutions of growing aggregates in these simulations. In all simulations of sequential collisions with constant impact velocities, the densities of aggregates decrease as the aggregates grow.

Comparison of the densities of the resultant aggregates with those of BCCA clusters is useful. For collisions at sufficiently low velocity, the BCCA structures are produced by the sticking together of equal-mass aggregates without any transformation. BCCA clusters have very fluffy structures and the fractal dimension of these aggregates is  $\simeq 2$ . The radius of gyration of BCCA clusters is given by (e.g., Mukai et al. 1992; W08)

$$r_{g,\text{BCCA}} \simeq N^{1/2} r_1. \quad (14)$$

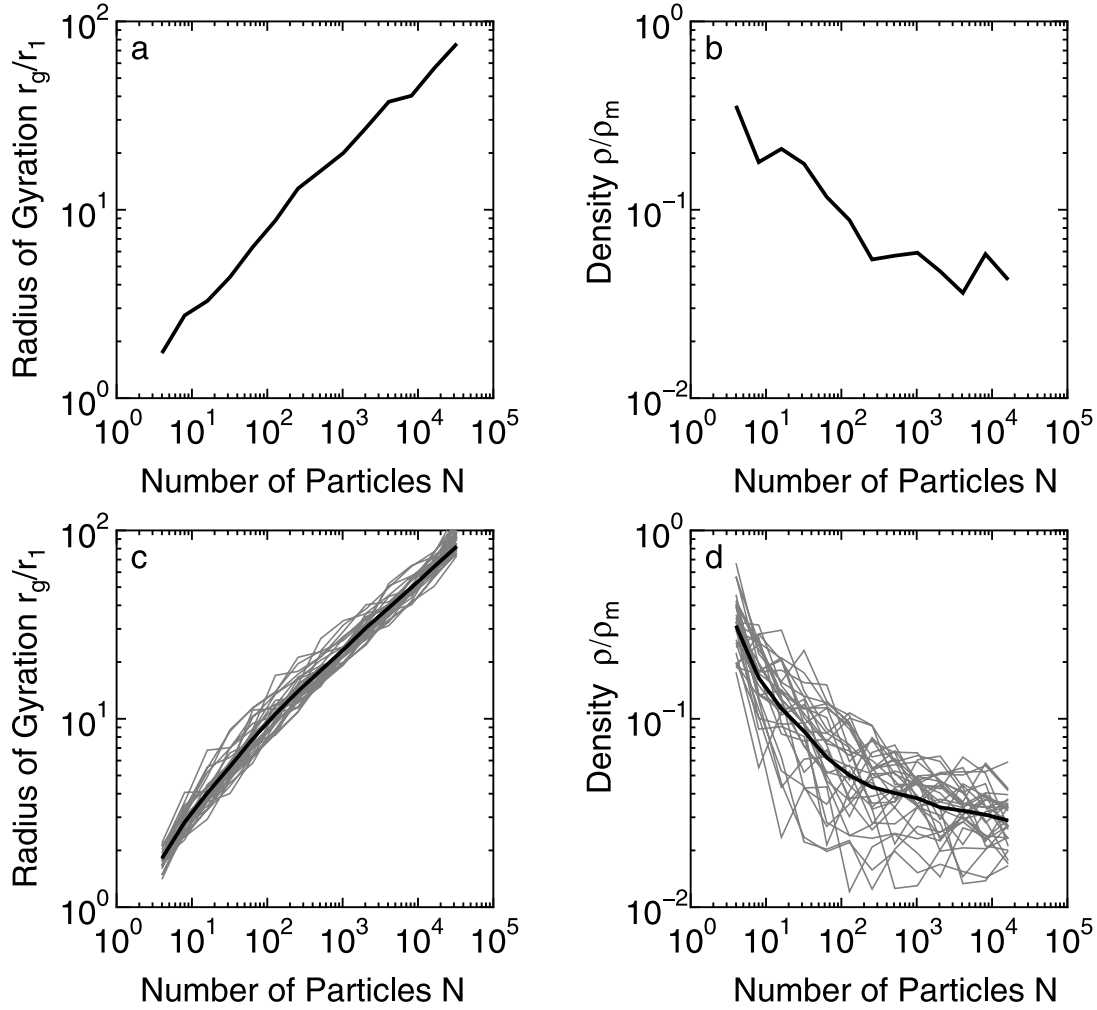


FIG. 4.—Radius of gyration and the density of the resultant aggregates in the case of  $v_{\text{imp}} = 0.54 \text{ m s}^{-1}$  and  $\xi_{\text{crit}} = 2 \text{ \AA}$  expressed as a function of the number of particles  $N$ . (a, b) Results for one run. (c, d) Results of 30 runs (gray lines) and the averaged radius of gyration and density (black lines). We obtain a smooth density evolution with this averaging.

Thus, the (average) density of BCCA clusters is evaluated to be

$$\rho_{\text{BCCA}} = \left(\frac{3}{5}\right)^{3/2} N^{-1/2} \rho_m, \quad (15)$$

where  $\rho_m [=3m_1/(4\pi r_1^3)]$  is the density of monomers. In Figure 5, dashed lines represent the density of BCCA clusters produced by W08, showing the same  $N$ -dependence as in equation (15) for large  $N$ . For small aggregates created in our simulation, their density changes along the curve of BCCA clusters. When the number of particles is larger than a critical value, the aggregates have a larger density than BCCA clusters due to compression at collisions. The beginning of compression can be estimated using  $E_{\text{imp}} \sim E_{\text{roll}}$  (Dominik & Tielens 1997; W08). Since the impact energy is given by

$$E_{\text{imp}} = \frac{1}{2} N m_1 \left(\frac{v_{\text{imp}}}{2}\right)^2, \quad (16)$$

in the center-of-mass system, the critical number of particles for compression is obtained as

$$N_{\text{crit}} = b \frac{8E_{\text{roll}}}{m_1 v_{\text{imp}}^2}, \quad (17)$$

where  $b$  is a nondimensional coefficient. In Figure 5, we also plot the critical number  $N_{\text{crit}}$  with filled circles on each density curve, by setting  $b = 0.5$ . Equation (17) with this value of  $b$  reproduces well the beginning of compression in the numerical results. W08 also confirmed the validity of equation (17) through their collisional simulation of BCCA clusters, but they obtained  $b = 0.15$  from their numerical results. This difference in  $N_{\text{crit}}$  means that the aggregates created here are somewhat stronger than BCCA clusters, even at the beginning of compression. In our simulation, the number of contact points of aggregates is larger than that of BCCA clusters by several percent at  $N = N_{\text{crit}}$ . This increase in the number of contact points would explain the strength of aggregate created in our simulation. After the density curves deviate from that for BCCA due to compression at collisions, the aggregate density continues to decrease in all cases.

We examine the fractal dimension of resultant aggregates as described in W08. W08 counted the number of particles  $N_{\text{in}}$  in spheres with a radius  $r$  inside the aggregate. They took the centers of each particle in the aggregate as the centers of the spheres and obtained the average value  $\bar{N}_{\text{in}}$  from the counting for each sphere. The fractal dimension of the aggregate is obtained from the  $r$ -dependence of  $\bar{N}_{\text{in}}$ . For various compressed aggregates created in our simulations, we plot  $\bar{N}_{\text{in}}$  as a function of  $r$  with  $N > N_{\text{crit}}$  (Fig. 6). The left panel shows the results in the

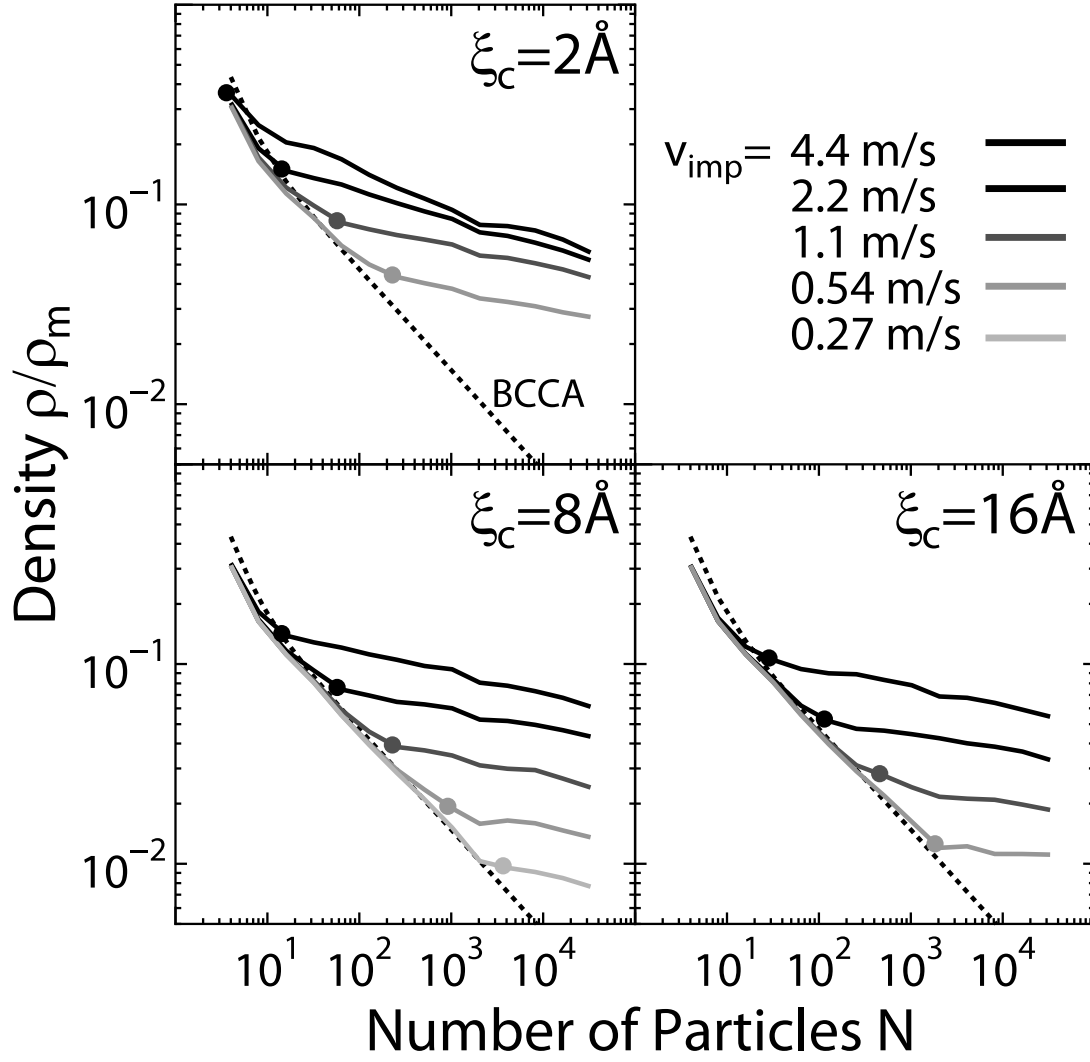


FIG. 5.—Density evolution of growing aggregates in the simulations for various impact velocities and critical rolling displacements. We set  $v_{\text{imp}} = 0.27, 0.54, 1.1, 2.2$ , and  $4.4 \text{ m s}^{-1}$  and  $\xi_{\text{crit}} = 2, 8, 16 \text{ \AA}$ . The solid lines show the densities of the resultant aggregates in our simulations, and the dashed lines indicate the densities of BCCA clusters. Filled circles indicate the critical number of particles  $N_{\text{crit}}$  to start compression, as estimated from eq. (17) with  $b = 0.5$ .

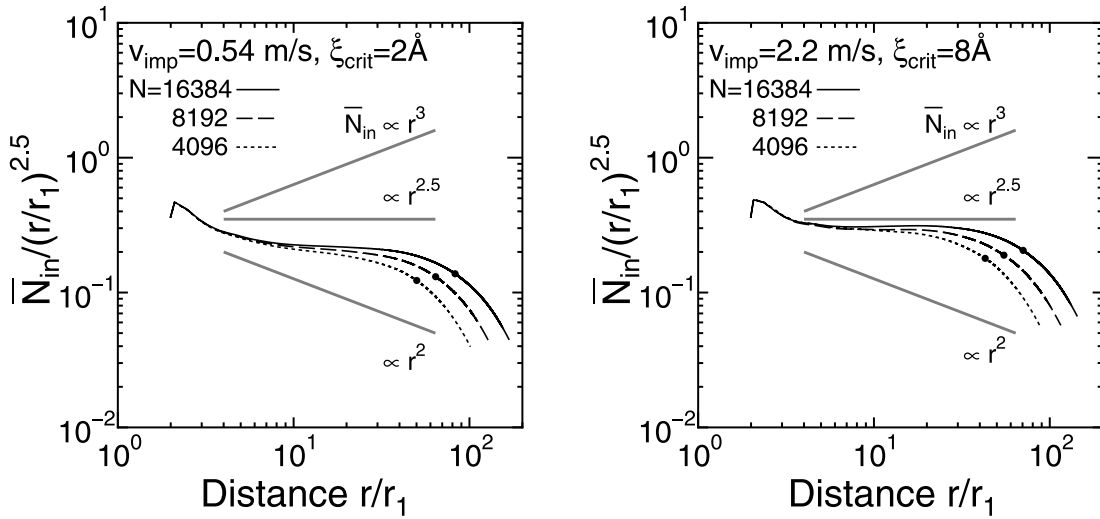


FIG. 6.—Average number of particles in spheres of radii  $r_{\text{in}}$  inside resultant aggregates with  $N > N_{\text{crit}}$ . *Left*, Case of  $v_{\text{imp}} = 0.54 \text{ m s}^{-1}$  and  $\xi_{\text{crit}} = 2 \text{ \AA}$ ; *right*, case of resultant aggregates formed by collisions with  $v_{\text{imp}} = 2.2 \text{ m s}^{-1}$  and  $\xi_{\text{crit}} = 8 \text{ \AA}$ . The dotted lines, dashed lines, and solid lines represent aggregates with  $N = 4096, 8192$ , and  $16384$ , respectively. Since the vertical axis is  $\bar{N}_{\text{in}}$  divided by  $(r/r_1)^{2.5}$ , the horizontal slope indicates  $\bar{N}_{\text{in}} \propto r^{2.5}$ , which means that the compressed aggregates have the fractal dimension of 2.5. The filled circles show the scale of the radius of gyration. In the range of  $4r_1 < r < r_g$ ,  $\bar{N}_{\text{in}}$  is approximately proportional to  $r^{2.5}$  for all aggregates, which indicates that the aggregates have the fractal dimension of 2.5.

case of  $v_{\text{imp}} = 0.54 \text{ m s}^{-1}$  and  $\xi_{\text{crit}} = 2 \text{ \AA}$ , and the right panel shows the results in the case of  $v_{\text{imp}} = 2.2 \text{ m s}^{-1}$  and  $\xi_{\text{crit}} = 8 \text{ \AA}$ . In the range of  $4r_1 < r < r_g$ ,  $N_{\text{in}}$  is approximately proportional to  $r^{2.5}$  for all aggregates (although  $N_{\text{in}}$  deviates from this trend for  $r > r_g$  due to the surface effect). Thus, as in W08, the compressed aggregates have the fractal dimension of 2.5 in our simulation. In our simulations, aggregates are gradually compressed by sequential collisions, while BCCA clusters are compressed by one collision in W08. This difference in the mode of compression does not affect the fractal dimension of the resultant aggregates. Since the compressed aggregates have the fractal dimension of 2.5, W08 introduced the fractal volume and the fractal pressure and modeled the aggregate compression. This model by W08 is expected to be applicable to the compression in sequential collisions, despite the difference in the compression mode. In § 4, we compare our results with the compression model by W08, and we further develop a model on the density evolution of growing aggregates.

#### 4. DENSITY EVOLUTION MODEL

##### 4.1. Compression with W08

W08 examined the compression process through the 3D numerical simulation of collisions between BCCA clusters. They obtained an “equation of state” of aggregates and succeeded in reproducing the aggregate compression in their numerical simulations with the use of the equation of state. We briefly describe the equation of state and investigate whether the obtained results of sequential collisions are well described by the equation of state. For the description of the resultant aggregates with the fractal dimension of 2.5, W08 introduced the fractal volume and the fractal density defined by

$$V_f \equiv ar_g^{2.5}, \quad (18)$$

$$\rho_f \equiv \frac{m_1 N}{V_f} = \frac{m_1 N}{a} r_g^{-2.5}, \quad (19)$$

where the coefficient  $a$  is given by  $(9\pi/5)^{5/4}/\Gamma(9/4) \simeq 7.7$ . The dimensions of the fractal volume and the fractal density differ from those of the ordinary volume and density. Based on these definitions, however, the fractal volume is an extensive variable ( $\propto N$ ) and the fractal density is an intensive variable for aggregates with the fractal dimension of 2.5. Thus, it is natural to use these fractal variables to describe the structure of the resultant aggregates.

As the impact energy  $E_{\text{imp}}$  increases, the resultant aggregate is compressed and its fractal volume  $V_f$  decreases. The small changes  $dE_{\text{imp}}$  and  $dV_f$  satisfy the relation

$$dE_{\text{imp}} = -P_f dV_f, \quad (20)$$

where the positive coefficient  $P_f$  is defined as the fractal pressure. W08 obtained the following formula of the fractal pressure from their numerical results

$$P_f = 0.60 \frac{E_{\text{roll}} \rho_{f,1}}{m_1} \left( \frac{\rho_f}{\rho_{f,1}} \right)^5, \quad (21)$$

where  $\rho_{f,1}$  is given by  $m_1/(ar_1^{2.5})$ . Integrating equation (20) with equation (21), we obtain the fractal volume of the resultant aggregate as a function of  $E_{\text{imp}}$ , which reproduces the nu-

merical results reported by W08 with high accuracy. Since  $\rho_f$  is an intensive variable, the fractal pressure  $P_f$  is also an intensive variable, and its dimension differs from that of the ordinary pressure.

Equation (21) can be expressed with the ordinary variables. The ordinary volume  $V$  and density  $\rho$  are defined by equations (12) and (13) and are expressed as

$$\frac{V}{V_m} = \left( \frac{5}{3} \right)^{3/2} \left( \frac{V_f}{V_{f,1}} \right)^{6/5}, \quad (22)$$

$$\frac{\rho}{\rho_m} = \left( \frac{3}{5} \right)^{3/2} \left( \frac{\rho_f}{\rho_{f,1}} \right)^{6/5} N^{-1/5}, \quad (23)$$

where  $V_m (=4/3\pi r_1^3)$  is the volume of a monomer and  $V_{f,1}$  is given by  $ar_1^{2.5}$ . The ordinary pressure is given by (see the Appendix of W08, for details)

$$P = 6.4 \frac{E_{\text{roll}} \rho_m}{m_1} \left( \frac{\rho}{\rho_m} \right)^{13/3} N^{2/3}. \quad (24)$$

Then, the relation,  $dE_{\text{imp}} = -P dV$ , also reproduces the numerical results. Note that the ordinary pressure depends not only on the density but also on the number of particles. Since the fractal dimension of the resultant aggregates in our simulations is the same as that reported in W08, their compression model is expected to be applicable to the resultant aggregates of the present study.

The density evolution due to collisions can be divided into two steps. In step 1, two aggregates, each of which is produced by the  $(i-1)$ th collision and has a fractal density of  $\rho_{f,i}$ , stick to each other at one contact point, and large voids are created, as shown in Figure 1b.

Then, the aggregate density decreases from  $\rho_{f,i}$  to  $\rho'_{f,i+1}$ . In step 2, the merged aggregate is compressed after sticking, and the resultant aggregate produced at the  $i$ th collision has an increased fractal density of  $\rho_{f,i+1}$ , as shown in Figure 1c. The density increases (from  $\rho'_{f,i+1}$  to  $\rho_{f,i+1}$ ) in step 2 is dependent on the impact energy, which is expected to be described by equations (20) and (21).

In a collision with a sufficiently low velocity, the density increase in step 2 is negligible, and the density decreases at the same rate as in BCCA clusters. The radius of gyration increases by the factor  $\sqrt{2}$  at each collision, because equation (14) is always true for BCCA clusters. Thus, using equation (19), the fractal density of the resultant aggregate produced at the  $i$ th collision is given by  $\rho_{f,i+1} = 2^{-1/4} \rho_{f,i}$ . Based on the assumption that the density change in step 1 is the same as that for BCCA clusters, we obtain

$$\rho'_{f,i+1} = 2^{-1/4} \rho_{f,i}. \quad (25)$$

The density change in step 2 is expressed by the integration of equation (20),

$$\begin{aligned} E_{\text{imp}} &= - \int_{V'_{f,i+1}}^{V_{f,i+1}} P_f dV_f \\ &= m_1 N_{i+1} \int_{\rho'_{f,i+1}}^{\rho_{f,i+1}} \frac{P_f}{\rho_f^2} d\rho_f, \end{aligned} \quad (26)$$

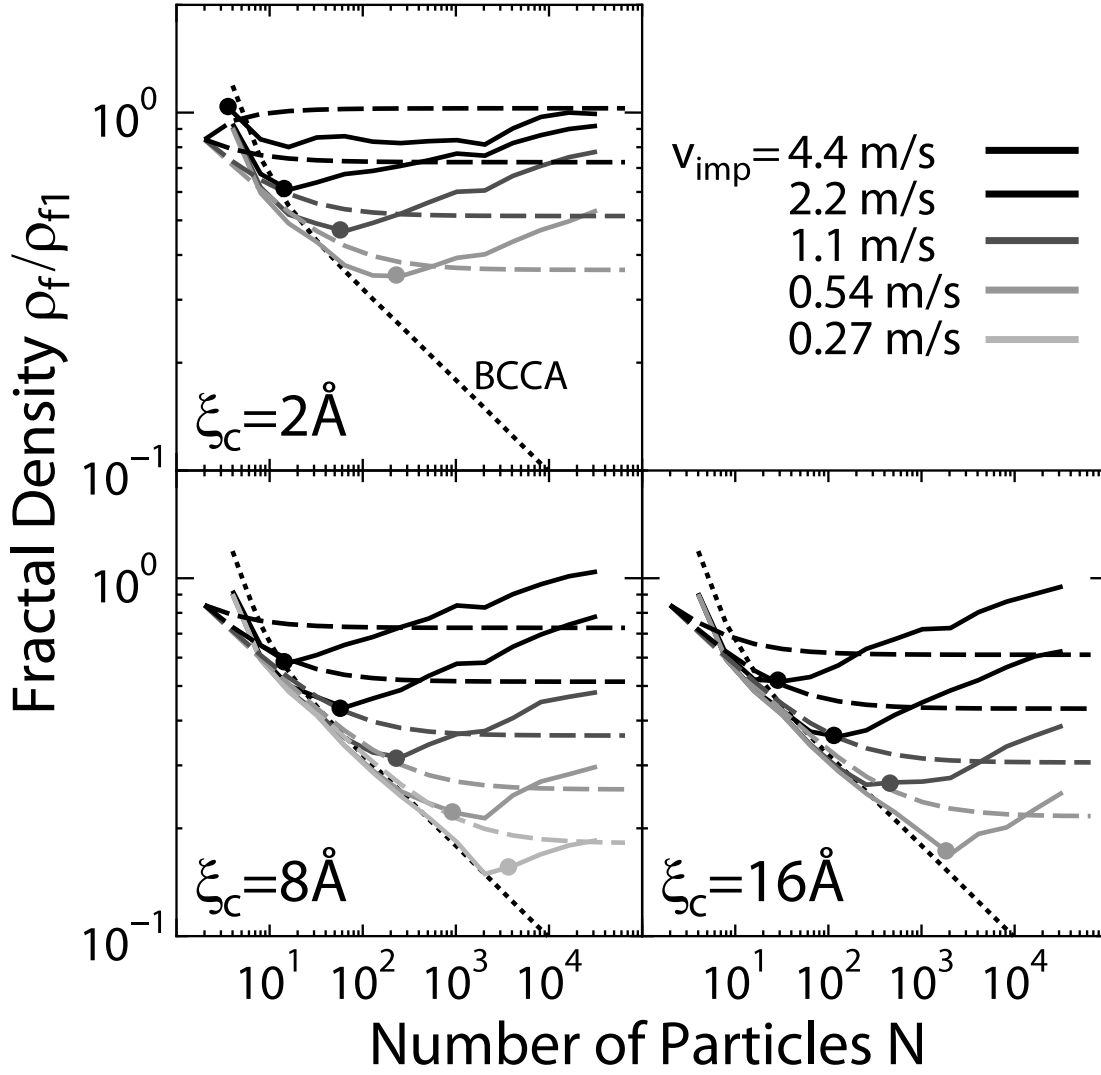


FIG. 7.— Comparison between the model of eq. (27) (dashed lines) and the numerical results (solid lines). The dotted lines show the density of BCCA clusters, and the filled circles indicate the critical number of particles  $N_{\text{crit}}$ .

where  $N_{i+1}$  is the number of particles, and  $V_{f,i+1}$  is the fractal volume of the resultant aggregate produced at the  $i$ th collision. In equation (26),  $V'_{f,i+1}$  is the fractal volume of the aggregate at the moment of sticking (i.e.,  $V'_{f,i+1} = m_1 N_{i+1} / \rho'_{f,i+1}$ ). Substituting equation (21) into equation (26) and using equation (25), we obtain the fractal density of the resultant aggregate produced at the  $i$ th collision as

$$\left(\frac{\rho_{f,i+1}}{\rho_{f,1}}\right)^4 = \frac{1}{2} \left(\frac{\rho_{f,i}}{\rho_{f,1}}\right)^4 + \frac{E_{\text{imp}}}{0.15 N_{i+1} E_{\text{roll}}}. \quad (27)$$

With this recurrence formula, we can obtain the fractal density of growing aggregates.

In Figure 7, we plot the fractal densities obtained from equation (27) (dashed line) and our numerical results (solid line). Note that  $\rho_f$  increases with  $N$  (Fig. 8), while  $\rho$  decreases with  $N$  (Fig. 5). Since  $\rho$  is proportional to  $N^{-1/5}$ ,  $\rho$  decreases even if  $\rho_f$  increases. Equation (27) does not agree with the numerical results. There are two types of deviation between the curves obtained from equation (27) and from the numerical results. The first type is related to the beginning of compression, and the second type is the slope of the density curves after the beginning of compression.

The critical number of particles  $N_{\text{crit}}$ , which indicates the position of the beginning of compression, is larger for our numerical results than for the model of W08. This delay in our results can be explained by the increase in the number of contact points in the aggregates at the beginning of compression, as discussed in § 3 (referring to the value of  $b$  in eq. [17]). The deviation in the slope of the fractal density is more serious because this causes a large error in the density for very large aggregates. For large aggregates, the fractal density obtained from equation (27) is constant, while that obtained from the numerical results increases. This indicates that the aggregates described by equation (27) are less compressible than those in our simulation. This deviation is due to an overestimation in the compression energy of the right-hand side of equation (26), as discussed in § 4.2.

#### 4.2. A Modified Model on Density Evolution

We examine the reason for the deviation in the slope (i.e., the compressibility of aggregates) for  $N > N_{\text{crit}}$  and construct a better compression model. At the moment of sticking in the next collision, large voids are created in the merged aggregate, which decreases the fractal density from  $\rho_{f,i}$  to  $\rho'_{f,i+1}$  as per step 1. If these voids are crushed after the sticking, the fractal density of



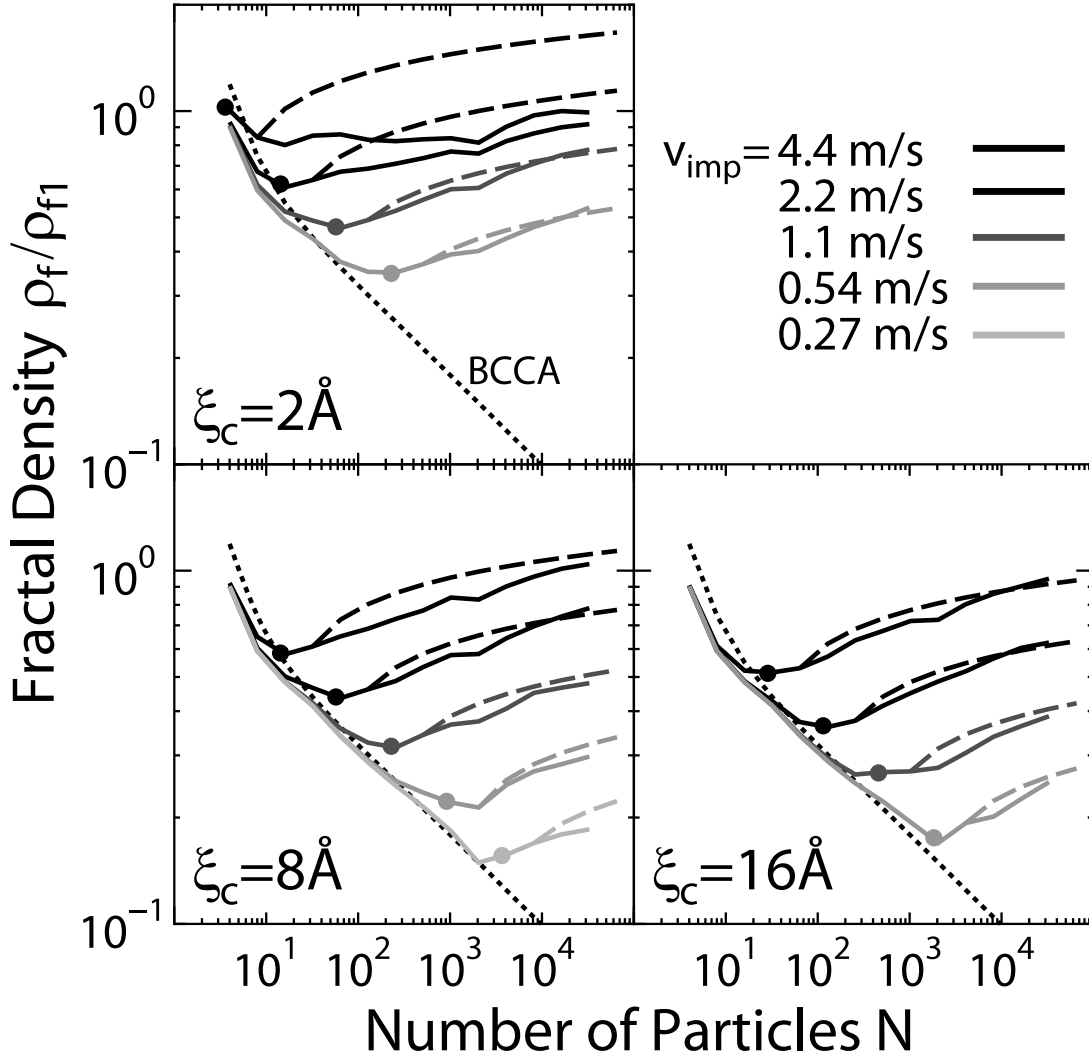


FIG. 8.—Comparison between the model of eq. (30) (*dashed lines*) and the numerical results (*solid lines*). The curves generated by eq. (30) start from  $N \simeq 2N_{\text{crit}}$ .

the aggregate will return to the value of  $\rho_{f,i}$ . The new voids would be crushed through rolling at several contact points in the aggregate, which requires the energy of only several  $E_{\text{roll}}$ . In equation (26), on the other hand, the energy required for the compression from  $\rho'_{f,i+1}$  to  $\rho_{f,i}$  is calculated, using equations (14), (19), and (25) as

$$m_1 N_{i+1} \int_{\rho'_{f,i+1}}^{\rho_{f,i}} \frac{P_f}{\rho_f^2} d\rho_f \sim \left( \frac{r_{g,\text{BCCA}}}{r_{g,i}} \right)^{10} E_{\text{roll}}, \quad (28)$$

where  $r_{g,i}$  is the radius of gyration of the resultant aggregate produced at the  $i$ th collision. Equation (28) indicates that the energy required for the crushing of the new voids is much larger than  $E_{\text{roll}}$  for the compressed aggregates with  $r_{g,i} < r_{g,\text{BCCA}}$ . Since such a large amount of energy is required for crushing of new voids, the fractal density does not increase in the compression model by W08 (see Fig. 7).

The increase in the fractal density in our numerical simulation indicates that the energy required for the compression to  $\rho_{f,i}$  might be negligibly small. On the other hand, once the fractal density increases to  $\rho_{f,i}$  due to crushing of the new voids, further compression is well described by  $P_f$  derived by W08. If the

energy for the compression to  $\rho_{f,i}$  is negligible, equation (26) is changed as

$$E_{\text{imp}} = m_1 N_{i+1} \int_{\rho_{f,i}}^{\rho'_{f,i+1}} \frac{P_f}{\rho_f^2} d\rho_f. \quad (29)$$

Note that the lower limit of the integral in equation (29) is  $\rho_{f,i}$ , but is  $\rho'_{f,i+1}$  in equation (26). Integrating the right-hand side of equation (29) with equation (21), we obtain another recurrence formula:

$$\left( \frac{\rho_{f,i+1}}{\rho_{f,1}} \right)^4 = \left( \frac{\rho_{f,i}}{\rho_{f,1}} \right)^4 + \frac{E_{\text{imp}}}{0.15 N_{i+1} E_{\text{roll}}}. \quad (30)$$

Note that this recurrence formula is invalid for collisions of almost uncompressed aggregates because we neglect the energy for crushing of the new voids. Since this energy is comparable to  $E_{\text{roll}}$ , equation (30) is valid only for collision with  $E_{\text{imp}} > E_{\text{roll}}$ , which is satisfied for collisions of aggregates with  $N > N_{\text{crit}}$  in our simulations. Figure 8 shows a comparison between the curves of equation (30) (*dashed lines*) and the numerical results (*solid lines*). Equation (30) reproduces well the numerical results for  $N \geq N_{\text{crit}}$ . When  $\rho_f/\rho_{f,1} \simeq 1$ , as seen in the case of  $\xi_{\text{crit}} = 2 \text{ \AA}$ ,

the fractal density of the numerical results deviates from the curve by equation (30). This is because  $\rho_{f,1}$  is the upper limit of  $\rho_f$  and the structure of  $\rho_f/\rho_{f,1} \simeq 1$  corresponds to the maximum compression. Therefore, we can conclude that, for collisions of  $E_{\text{imp}} > E_{\text{roll}}$ , the energy required for the compression to  $\rho_{f,i}$  is negligibly small as long as  $\rho_f/\rho_{f,1} < 1$  and that equation (30) is valid for such collisions.

For further investigation of the density evolution of aggregates, we transform equation (30) to the following form:

$$\frac{d}{dN} \left[ \left( \frac{\rho_f}{\rho_{f,1}} \right)^4 \right] = \frac{1}{0.15(\ln 2)N} \frac{E_{\text{imp}}}{NE_{\text{roll}}}, \quad (31)$$

where we used the relation  $N_i = 2^{i-1}$ . Using equation (23), we further rewrite equation (31), in terms of the ordinary density, as

$$\begin{aligned} \frac{d \ln \rho}{d \ln M} = & -\frac{1}{5} + \frac{0.16}{\ln 2} \left( \frac{M}{m_1} \right)^{-2/3} \\ & \times \left( \frac{\rho}{\rho_m} \right)^{-10/3} \frac{E_{\text{imp}}}{NE_{\text{roll}}}, \end{aligned} \quad (32)$$

where  $M (\equiv m_1 N)$  is the mass of the aggregate. This equation describes the density evolution of growing aggregates. The second term in the right-hand side represents the compression of aggregates through rolling. On the other hand, the first term of the right-hand side reduces the aggregate density. This term comes from the fact that, for aggregates growing with the fractal dimension of 2.5 (or with a constant fractal density), their ordinary density decreases as  $\propto M^{-1/5}$  (see eq. [23]). Because of this first term, the aggregate density decreases even for collisions with  $E_{\text{imp}} \gg E_{\text{roll}}$ , as shown in Figure 5. On the other hand, if the second term is larger than 1/5, the aggregate density increases with growth. Such a case occurs for aggregates with a sufficiently low density. Thus, the aggregate density is regulated so that the right-hand side of equation (32) converges to a certain value. Assuming  $\rho \propto M^\beta$ , we obtain the density of growing aggregates as

$$\rho = \left[ \frac{0.16}{\ln 2(\beta + 1/5)} \frac{E_{\text{imp}}}{NE_{\text{roll}}} \right]^{3/10} \left( \frac{M}{m_1} \right)^{-1/5} \rho_m. \quad (33)$$

To fix the exponent  $\beta$ , the  $M$ - and  $\rho$ -dependence of  $E_{\text{imp}}$  is needed. However, equation (33) is useful for order estimation of the aggregate density. Note that if the impact velocity is constant,  $\rho$  is proportional to  $M^{-1/5}$  and  $\beta$  is  $-1/5$ . In this case, we should solve equation (32) to obtain the correct solution because equation (33) diverges. Although equations (32) and (33) are based on numerical simulations of icy aggregate collisions, these equations are also applicable to the compression of silicate aggregates by the use of  $E_{\text{roll}}$  of silicate.

Ormel et al. (2007) developed a simple compression model and examined the density evolution of growing aggregates with their model. In their model, they assumed that aggregates are compressed up to the material density  $\rho_m$  when the impact energy reaches  $NE_{\text{roll}}$ . Although this assumption seems reasonable, based on our numerical results, equation (32) (or eq. [33]) indicates that huge aggregates have much lower densities than  $\rho_m$  even when  $E_{\text{imp}} \sim NE_{\text{roll}}$ . In the present study, we only examined aggregate compression through head-on collisions. The effect of oblique collisions would further reduce the aggregate density.

## 5. IMPLICATION FOR DUST GROWTH IN PROTOPLANETARY DISKS

In § 4.2, we derived the equation describing the density evolution of growing dust aggregates (eq. [33]). We apply this to the growth of icy dust aggregates in protoplanetary disks. To examine the density evolution with equation (33), we need the expression of impact velocities between dust aggregates. We first briefly describe the motion of dust aggregates in protoplanetary disks.

Since dust aggregates are coupled with disk gas, the aggregates rotate around the central star together with the disk gas. The relative velocity between dust aggregates and the gas disk is determined by the balance between the gravitational force from the central star and the gas drag force. To describe the disk, we use a cylindrical coordinate system  $(R, \phi, z)$ , the origin of which is located at the central star. The  $z$ -axis coincides with the rotation axis of the disk. We consider a laminar disk and adopt the minimum-mass solar nebula model (Hayashi 1981). In this disk model, the gas surface density  $\Sigma_g$  is given by  $2 \times 10^4 (R/1 \text{ AU})^{-3/2} \text{ kg m}^{-2}$ , and the disk temperature  $T$  is given by  $3 \times 10^2 (R/1 \text{ AU})^{-1/2} \text{ K}$ .

The relative velocity between dust aggregates and gas is written as a function of the stopping time,  $t_{\text{stop}}$  (e.g., Weidenschilling 1977; Nakagawa et al. 1986). The stopping time is the time in which the velocity of dust aggregates relax to the gas velocity. The vertical and radial components of the relative velocity are given as follows:

$$v_z = t_{\text{stop}} \Omega_K \frac{z}{h} c_s, \quad (34)$$

$$v_R = \frac{2t_{\text{stop}} \Omega_K}{1 + (t_{\text{stop}} \Omega_K)^2} \eta v_K, \quad (35)$$

where  $\Omega_K$  is the Keplerian angular velocity,  $c_s$  is the speed of sound, and  $h (\equiv c_s/\Omega_K)$  is the gas scale height. In equation (35),  $\eta v_K$  is the difference between the Keplerian velocity  $v_K$  and the gas rotational velocity. A small nondimensional number  $\eta$  is given by  $-1/(2R\Omega_K^2 \rho_g)(\partial P_g/\partial R)$ , where  $P_g$  is the gas pressure and  $\rho_g$  is the gas density. In the minimum-mass solar nebula model,  $c_s$  is given by  $10^3 (R/1 \text{ AU})^{-1/4} \text{ m s}^{-1}$  and  $\eta v_K$  is given by  $50 \text{ m s}^{-1}$ .

The expression of the stopping time is divided into two cases, depending on the dust size  $r_{\text{crit}}$  and the mean free path of disk gas  $l_g$  (Adachi et al. 1976; Tanaka et al. 2005). The mean free path is given by  $(\mu m_u/\sigma_{\text{mol}})/\rho_g$ , where  $m_u$  is the atomic mass unit,  $\mu$  ( $=2.34$ ) is the mean molecular weight of disk gas, and  $\sigma_{\text{mol}}$  ( $=2 \times 10^{-19} \text{ m}^2$ ) is the molecular collision cross section. For  $r_{\text{crit}} \leq 3l_g/2$ , the gas drag is described by Epstein's law, and the stopping time is given by

$$t_{\text{stop}} \simeq \frac{1}{\Sigma_g \Omega_K} \frac{M}{S}, \quad (36)$$

where  $S$  is the cross section of the dust aggregate. On the other hand, for  $r_{\text{crit}} > 3l_g/2$ , the gas drag force is given by Stokes' law and the stopping time is given by

$$t_{\text{stop}} \simeq \frac{1}{\rho_g l_g h \Omega_K} \frac{M r_{\text{crit}}}{S}. \quad (37)$$

We consider dust growth through collisions between aggregates with comparable sizes mentioned in § 4. On the collision between aggregates that have the same density and the same size, the impact velocity vanishes. However, a variety of densities and sizes between aggregates of comparable size would result in the impact velocity being comparable with the relative velocity

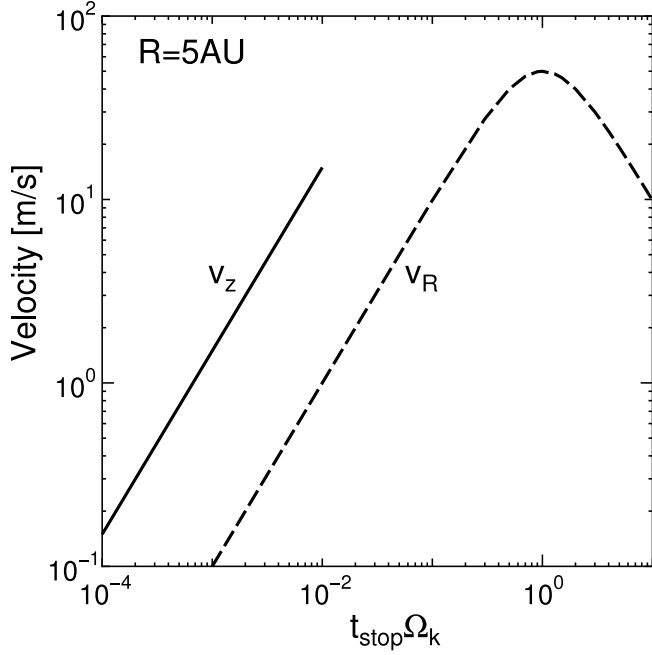


FIG. 9.— Relative velocity of dust aggregates with respect to the gas disk as a function of  $t_{\text{stop}}\Omega_K$ . The solid line shows the vertical velocity  $v_z$  at  $z = h$ , and the dashed line shows the radial velocity,  $v_R$ . At  $z = h$ , the impact velocity is given by  $v_z$ . For  $t_{\text{stop}}\Omega_K > 0.01$ , dust aggregates settle to the midplane of the disk, and the impact velocity is given by  $v_R$ . At  $t_{\text{stop}}\Omega_K = 1$ ,  $v_R$  attains the maximum value of 50 m s<sup>-1</sup>.

between aggregates and gas. Figure 9 shows the relative velocity of dust aggregates to the gas disk as a function of  $t_{\text{stop}}$  at  $R = 5$  AU. As dust aggregates grow and are compressed through collisions, the vertical and radial velocities increase because an increase in the ratio  $M/S$  due to compression increases their stopping times. Before settling (e.g.,  $z \sim h$ ),  $v_z$  is larger than  $v_R$  and the impact velocity is approximately given by  $v_z$ . Dust aggregates settle to the midplane of the disk for  $t_{\text{stop}}\Omega_K > 0.01$  (Safronov 1969; Tanaka et al. 2005), and the impact velocity is then approximately given by  $v_R$ . The radial velocity  $v_R$  increases further with  $t_{\text{stop}}$  and attains its maximum value of  $\eta v_K$  at  $t_{\text{stop}}\Omega_K = 1$ .

By substituting the formula for the impact velocity (eqs. [34] or [35]) into equation (33), we can examine the density evolution. The velocity changes as the amount of dust grows in protoplanetary disks, while the impact velocity was assumed to be constant in our simulation. In both cases, however, the density evolution is similar. That is, aggregates first grow as BCCA clusters, because of their low impact velocities. When the number of particles is larger than the critical value of  $N_{\text{crit}}$ , the aggregates begin to be compressed. Then, the density is higher than that of BCCA clusters. We evaluate the critical number  $N_{\text{crit}}$  for dust aggregates in the protoplanetary disk. For BCCA clusters, the size  $r_{\text{crit}}$  is approximately proportional to  $M^{1/2}$ . Thus, assuming  $S = \pi r_{\text{crit}}^2$ , we find that the ratio  $M/S$  is approximately constant. Therefore, the impact velocity of BCCA clusters is the same as that of 0.1  $\mu\text{m}$  sized monomers. Substituting the impact velocity formula into equation (17), we obtain  $N_{\text{crit}}$  as

$$N_{\text{crit}} \sim b \frac{8E_{\text{roll}}}{m_1 t_{\text{stop}}^2 \Omega_K^2 c_s^2} \sim 2 \times 10^{11} \left( \frac{\xi_{\text{crit}}}{10 \text{ \AA}} \right) \left( \frac{R}{5 \text{ AU}} \right)^{-5/2}, \quad (38)$$

where we used  $b = 0.5$ . In the above, we calculated  $t_{\text{stop}}$  for 0.1  $\mu\text{m}$  sized monomers and assumed that the compression begins at  $z = h$  and used Epstein's law (eq. [36]). Using equation (14), the critical radius is given by

$$r_{\text{crit}} = N_{\text{crit}}^{1/2} r_1 \sim 4 \left( \frac{\xi_{\text{crit}}}{10 \text{ \AA}} \right)^{1/2} \left( \frac{R}{5 \text{ AU}} \right)^{-5/4} \text{ cm}. \quad (39)$$

Since  $r_{\text{crit}}$  is smaller than the mean free path ( $\sim 1$  m) at 5 AU, Epstein's law is valid. Similar estimation was performed by Blum (2004). Note that his estimation differs from our estimation because of differences in the monomer radius and the fitting parameter  $b$ .

After the aggregate compression begins, the density becomes higher than that of BCCA clusters and  $t_{\text{stop}}$  increases. When  $t_{\text{stop}}\Omega_K = 1$ , the impact velocity becomes maximum and the aggregates are most compressed at this point. We consider the density evolution of aggregates in the disk midplane after their settling to examine the density of the most compressed aggregates. Thus, the impact velocity is approximately given by  $v_R$ . Since we are interested in the density evolution up to  $t_{\text{stop}}\Omega_K \simeq 1$ , the radial velocity is approximately given by

$$v_R \simeq 2t_{\text{stop}}\Omega_K \eta v_K. \quad (40)$$

From the definition of the density (eqs. [12] and [13]), the size  $r_{\text{crit}}$  and the cross section  $S (= \pi r_{\text{crit}}^2)$  are written as functions of the density and the mass by

$$r_{\text{crit}} \sim \left( \frac{M}{\rho} \right)^{1/3}, \quad (41)$$

$$S \sim \left( \frac{M}{\rho} \right)^{2/3}, \quad (42)$$

respectively. We further assume Stokes' law for gas drag. Substituting equations (41) and (42) into equations (37) and (40), the impact velocity is obtained as

$$v_{\text{imp}} \simeq \frac{2}{\rho_g l_g h} M^{2/3} \rho^{1/3} \eta v_K. \quad (43)$$

Using this expression of the impact velocity and equation (33), we solve the coupled evolution of the aggregate density and the impact velocity. Finally, we have the aggregate density and the impact velocity as

$$\rho \sim \rho_{\text{max}} \left( \frac{M}{M_{\text{max}}} \right)^{1/4}, \quad (44)$$

$$v_{\text{imp}} \sim \eta v_K \left( \frac{M}{M_{\text{max}}} \right)^{3/4}, \quad (45)$$

where the density  $\rho_{\text{max}}$  and the mass  $M_{\text{max}}$  of the most compressed aggregates at  $t_{\text{stop}}\Omega_K = 1$  are given by

$$\rho_{\text{max}} \sim \left[ \frac{m_1 (\eta v_K)^2}{E_{\text{roll}}} \right]^{1/3} \left( \frac{\rho_m r_1^2}{\rho_g l_g h} \right)^{1/3} \rho_m, \quad (46)$$

$$M_{\text{max}} \sim \left[ \frac{m_1 (\eta v_K)^2}{E_{\text{roll}}} \right]^{-1/6} \left( \frac{\rho_m r_1^2}{\rho_g l_g h} \right)^{-5/3} m_1. \quad (47)$$

TABLE 1  
VALUES OF  $\rho_{\max}$ ,  $M_{\max}$ , AND  $r_{\max}$  AT  $R = 5$  AU AND  $\xi_{\text{crit}} = 10 \text{ \AA}$

Material	$\rho_m$ ( $\text{kg m}^{-3}$ )	$\gamma$ ( $\text{mJ m}^{-2}$ )	$\rho_{\max}$ ( $\text{kg m}^{-3}$ )	$M_{\max}$ (kg)	$r_{\max}$ (m)
Ice.....	1000	100	$\sim 0.1$	$\sim 10^5$	$\sim 100$
Silicate.....	2600	25	$\sim 1$	$\sim 10^5$	$\sim 100$

The radius  $r_{\max}$  of dust aggregates that have the maximum velocity is given by  $[3M_{\max}/(4\pi\rho_{\max})]^{1/3}$ . For the disk model we adopt,  $\rho_{\max}$ ,  $M_{\max}$ , and  $r_{\max}$  are approximately given by

$$\rho_{\max} \sim 0.1 \left( \frac{\xi_{\text{crit}}}{10 \text{ \AA}} \right)^{-1/3} \left( \frac{R}{5 \text{ AU}} \right)^{-5/12} \text{ kg m}^{-3}, \quad (48)$$

$$M_{\max} \sim 10^5 \left( \frac{\xi_{\text{crit}}}{10 \text{ \AA}} \right)^{1/6} \left( \frac{R}{5 \text{ AU}} \right)^{25/12} \text{ kg}, \quad (49)$$

$$r_{\max} \sim 100 \left( \frac{\xi_{\text{crit}}}{10 \text{ \AA}} \right)^{1/6} \left( \frac{R}{5 \text{ AU}} \right)^{5/6} \text{ m}. \quad (50)$$

Replacing  $\eta v_K$  by  $\Omega_K z$  in equations (46) and (47), we can also obtain the density evolution of dust before the settling. In the above, we assumed Stokes' law. Since the mean free path is 1 m at  $R = 5$  AU, this assumption is valid for  $r_{\text{crit}} > 1$  m.

The obtained aggregate density is extremely low compared with that of compact aggregates ( $10^3 \text{ kg m}^{-3}$ ), even for the most compressed aggregates with  $t_{\text{stop}}\Omega_K = 1$ . This low value of  $\rho_{\max}$  is also explained by the fact that compressed aggregates have a fractal dimension of 2.5. Aggregates with such an extremely low density would significantly change the formation process of planetesimals. For example, these aggregates have relatively large cross sections, which accelerates their collisional growth without self-gravity. In the above calculation, we considered only icy dust aggregates. However, using the material parameters of silicate ( $\rho_m$  and  $\gamma$ ), we can obtain  $\rho_{\max}$ ,  $M_{\max}$ , and  $r_{\max}$  for silicate dust aggregates (see Table 1). Because the surface energy of silicate aggregates is smaller than that of icy aggregates, the sticking force is weak and the inelastic rolling motion easily occurs. Thus, silicate aggregates are easily compressed and  $\rho_{\max}$  of silicate aggregates is higher than that of icy aggregates. For silicate aggregates  $M_{\max}$  and  $r_{\max}$  are almost same as that of icy aggregates. Note that for silicate aggregates collisional fragmentation prevents dust growth before the density reaches to  $\rho_{\max}$ , although we can obtain  $\rho_{\max}$  from equation (46).

If we consider large monomer particles, aggregates are compressed more easily and the density increases. Equation (46) depends on  $r_1$ ,  $m_1$ , and  $E_{\text{roll}}$ . The mass of particles  $m_1$  is proportional to  $r_1^3$ , while the rolling energy  $E_{\text{roll}}$  is proportional to  $r_1$  (see eq. [7]). Thus,  $\rho_{\max}$  is proportional to  $r_1^{4/3}$ . This means that aggregates consisting of large particles are easily compressed (e.g.,  $\rho_{\max}$  becomes  $\sim 1 \text{ kg m}^{-3}$  for aggregates with  $r_1 = 1 \text{ }\mu\text{m}$ ).

In the derivation of equation (33), we only considered head-on collisions of aggregates. The effect of oblique collisions may further reduce the aggregate density. Another factor we do not take account in our compression model is the influence of fragmentation of dust aggregates. Collisional fragmentation may be especially important for silicate aggregates because the maximum velocity  $\eta v_K$  is higher than the critical velocity for fragmentation. The critical velocity is given by  $\sim 10 \text{ m s}^{-1}$  for icy aggregates and  $\sim 1 \text{ m s}^{-1}$  for silicate aggregates (Dominik & Tielens 1997; W07; W08).

We considered the density evolution of dust aggregates in laminar disks. In turbulent disks, the impact velocity can be enhanced by turbulent gas motion (e.g., Völk et al. 1980; Ormel & Cuzzi 2007). If the  $\alpha$ -parameter (which is related to the strength of disk turbulence) is comparable to 0.01, the impact velocity is given by up to  $10^2 \text{ m s}^{-1}$ . If  $\alpha$  is large, the velocity becomes higher. In this case, the velocity enhancement due to disk turbulence further compresses dust aggregates, but may prevent their growth due to collisional disruption even for icy aggregates. If  $\alpha$  is small, the effect of turbulence may not be effective. The density evolution in turbulent disks can be also estimated by applying equation (33) with the enhanced velocity.

## 6. SUMMARY AND DISCUSSION

We examined the density evolution of growing aggregates through 3D  $N$ -body numerical simulations of sequential head-on collisions of icy aggregates. Our results are summarized as follows:

1. In our simulation of sequential collisions, aggregates first grow as BCCA clusters and then the aggregate density rapidly decreases. When  $E_{\text{imp}} \sim E_{\text{roll}}$ , aggregates begin to be compressed. This is basically consistent with the results of previous studies (Dominik & Tielens 1997; W07, W08). Even after the beginning of compression, the density continues to decrease in our simulation with a constant impact velocity.
2. The fractal dimension of the compressed aggregates is 2.5, which agrees with that of resultant aggregates obtained by W08. This relatively small fractal dimension explains the density decrease of growth compressed aggregates in our simulation.
3. The density evolution in our simulation of sequential collisions is not reproduced by the compression model reported by W08, because their model overestimates the energy required for crushing of the new voids created at each collision. By neglecting the energy for crushing the new voids, we succeeded in reproducing the density evolution in our simulation. Based on this result, we also derived an equation describing the density evolution of growing aggregates (eq. [32]). Although we considered only icy aggregates in our numerical simulation, our results on aggregate compression can be applied to silicate aggregates by using a suitable value of  $E_{\text{roll}}$ .
4. We applied our results on the density evolution to dust growth of icy aggregate in protoplanetary disks and found that aggregates have an extremely low density ( $< 0.1 \text{ kg m}^{-3}$ ; see eqs. [46] and [48]) because of their small fractal dimension of 2.5.

Note that our results are based on simulations of head-on collision. A grazing impact (i.e., high impact parameter) with an intermediate velocity results in an elongated aggregate (see Fig. 17 of W07). Thus, the effect of oblique collisions can be expected to further reduce the density of aggregates. This effect will be examined in a future study.

In the present study, we consider the collision between equal-sized aggregates. At a collision between large and small aggregates, the small one can penetrate into the voids of the large one, leading to a larger density than obtained at collisions between equal-sized aggregates. It is important to examine the collision between aggregates of a various sizes.

In protoplanetary disks, the ram pressure due to gas drag is also exerted on dust aggregates. Although in most cases the ram pressure is weak compared with the effective pressure (or the strength) of aggregates evaluated by W08, the ram pressure acts over a much longer period than the characteristic time of collisions ( $\sim \mu\text{s}$ ). Thus, the compression due to the ram pressure may be effective. For

sufficiently large aggregates, their self gravity would also be effective. Recently, Paszun & Dominik (2008) examined the compressive strength of small aggregates for static compression with numerical simulations and reproduced the results of laboratory experiments by Blum & Schräpler (2004). Further investigations on static compression should be performed for large aggregates with a very low density.

Moreover, in the present paper, we did not consider the effect of sintering. At the inner regions of protoplanetary disks, the sintering effect forms necks at the contact points between monomer particles in aggregates. This effect would stiffen the structure of aggregates. The stiff structure would prevent energy dissipation due to rolling motion, so that aggregates may break up easily on

collision. It is necessary to examine how sintering changes the strength and collisional outcomes of aggregates.

We thank an anonymous reviewer for useful comments. The authors would like to thank Tetsuo Yamamoto and Hiroshi Kimura for his valuable discussion. We would also like to thank Takeshi Chigai for technical support with respect to the computer setup. This study was supported in part by a Grant-in-Aid for Scientific Research on Priority Areas “Development of Extrasolar Planetary Science” (16077203) from MEXT, Japan, and by a Grant-in-Aid from JSPS (18540227, 20740247).

#### REFERENCES

- Adachi, I., Hayashi, C., & Nakazawa, K. 1976, *Prog. Theor. Phys.*, 56, 1756  
 Blum, J. 2004, in *ASP Conf. Ser. 309, Astrophysics of Dust*, ed. A. N. Witt, G. C. Clayton, & B. T. Draine (San Francisco: ASP), 369  
 Blum, J., & Schräpler, R. 2004, *Phys. Rev. Lett.*, 93, 115503  
 Blum, J., & Wurm, G. 2000, *Icarus*, 143, 138  
 Chokshi, A., Tielens, A. G. G. M., & Hollenbach, D. 1993, *ApJ*, 407, 806  
 Dominik, C., & Tielens, A. G. G. M. 1995, *Philos. Mag. A*, 72, 783  
 ———. 1996, *Philos. Mag. A*, 73, 1279  
 ———. 1997, *ApJ*, 480, 647  
 Goldreich, P., & Ward, W. R. 1973, *ApJ*, 183, 1051  
 Goldstein, H. 1950, *Classical Mechanics* (Reading: Addison-Wesley)  
 Hayashi, C. 1981, *Prog. Theor. Phys. Suppl.*, 70, 35  
 Heim, L.-O., Blum, J., Preuss, M., & Butt, H.-J. 1999, *Phys. Rev. Lett.*, 83, 3328  
 Johnson, K. L., Kendall, K., & Roberts, A. D. 1971, *Proc. R. Soc. London A*, 324, 301  
 Kempf, S., Pfalzner, S., & Henning, T. K. 1999, *Icarus*, 141, 388  
 Krause, M., & Blum, J. 2004, *Phys. Rev. Lett.*, 93, 021103  
 Meakin, P. 1991, *Rev. Geophys.*, 29, 317  
 Mukai, T., Ishimoto, H., Kozasa, T., Blum, J., & Greenberg, J. M. 1992, *A&A*, 262, 315  
 Nakagawa, K., Sekiya, M., & Hayashi, C. 1986, *Icarus*, 67, 375  
 Nakagawa, Y., Nakazawa, K., & Hayashi, C. 1981, *Icarus*, 45, 517  
 Ormel, C. W., & Cuzzi, J. N. 2007, *A&A*, 466, 413  
 Ormel, C. W., Spaans, M., & Tielens, A. G. G. M. 2007, *A&A*, 461, 215  
 Ossenkopf, V. 1993, *A&A*, 280, 617  
 Paraskov, G. B., Wurm, G., & Krauss, O. 2007, *Icarus*, 191, 779  
 Paszun, D., & Dominik, C. 2006, *Icarus*, 182, 274  
 ———. 2008, *A&A*, 484, 859  
 Poppe, T., Blum, J., & Henning, T. 2000, *ApJ*, 533, 454  
 Safronov, V. S. 1969, *Evolution of the Protoplanetary Cloud and Formation of the Earth and the Planets* (NASA TTF-677; Moscow: Nauka)  
 Tanaka, H., Himeno, Y., & Ida, S. 2005, *ApJ*, 625, 414  
 Völk, H. J., Jones, F. C., Morfill, G. E., & Röser, S. 1980, *A&A*, 85, 316  
 Wada, K., Tanaka, H., Suyama, T., Kimura, H., & Yamamoto, T. 2007, *ApJ*, 661, 320 (W07)  
 ———. 2008, *ApJ*, 677, 1296 (W08)  
 Weidenschilling, S. J. 1977, *MNRAS*, 180, 57  
 ———. 1980, *Icarus*, 44, 172  
 Weidenschilling, S. J., & Cuzzi, J. N. 1993, in *Protostars and Planets III*, ed. E. H. Levy & J. I. Lunine (Tucson: Univ. Arizona Press), 1031  
 Wurm, G., Paraskov, G., & Krauss, O. 2005, *Icarus*, 178, 253